

Manipulation of diamond nanoparticles using bulk acoustic waves

Bart Raeymaekers,^{a)} Cristian Pantea, and Dipen N. Sinha

Los Alamos National Laboratory, P.O. Box 1663, MS D429 Los Alamos, New Mexico 87545, USA

(Received 16 September 2010; accepted 20 November 2010; published online 11 January 2011)

We investigate the manipulation of 5 nm diamond nanoparticles in a user-defined pattern on a substrate using the acoustic radiation force associated with a bulk acoustic standing wave. Both concentric and rectangular patterns are studied and the experimental results are compared with theoretical predictions. The effect of drag force acting on a nanoparticle is evaluated and limits for particle speed and particle size that can be moved by acoustic radiation force are determined. We found good agreement between our experimental results and existing theoretical models and demonstrate that nanosized particles can be manipulated effectively by means of bulk wave acoustic radiation force. © 2011 American Institute of Physics. [doi:10.1063/1.3530670]

I. INTRODUCTION

The acoustic radiation force associated with a standing ultrasonic wave allows trapping of suspended particles in a host fluid at nodes or antinodes of that wave, depending on the compressibility and density of the particles and the host fluid.¹ The origin of the acoustic radiation force associated with a pressure wave is documented extensively in the literature.^{1–5} Woodside *et al.*⁶ used a microscope-based imaging system to experimentally quantify the direction and magnitude of the acoustic radiation force. They derived the acoustic radiation force from measured particle velocities under the assumption that the drag force is counterbalanced by the driving acoustic radiation force. In another publication, Woodside *et al.*⁷ discussed the effectiveness of particle/liquid separation by ultrasound radiation force, and found this to depend on the acoustic energy density distribution in the standing wave field. This could potentially enable designing optimized resonator cavities for specific particle/fluid separation applications.

Acoustic manipulation is commonly used in the area of microfluidics to separate or manipulate micrometer sized bacteria and/or cells (e.g., Refs. 8–10). It is also used to manipulate suspended particles in parallel planes or at the axis of a tube with standing waves in one direction.¹¹ Continuous separation of particles from fluid suspensions was first demonstrated by Tolt and Feke.¹² Acoustic radiation force has also been used to separate different particle sizes from each other. Mandralis *et al.*¹³ showed fractionalization based on particle size, while Gupta *et al.*¹⁴ devised a method for continuous fractionalization of mixed-particulate suspensions based on the compressibility of the solid phase. Jung *et al.*¹⁵ presented a microfluidic particle filter that relies on acoustic radiation force to remove particles that exceed a predefined size. They studied particles in the range of 0.5–5 μm . Multidimensional acoustic manipulation of microparticles has been achieved by Oberti *et al.*,¹⁶ who created orthogonal-superimposed standing pressure waves in a micromachined fluidic chamber to manipulate 9.6 μm particles in two-dimensional patterns. Smaller microparticles with a

diameter of 0.5 μm were manipulated into so-called Chladni patterns by means of a vibrating cantilever beam in a microfluidic cell by Dorrestijn *et al.*¹⁷ Most recently, Mazzocchi *et al.*¹⁸ employed acoustic manipulation to aggregate mammalian cells in annuli of 80 μm , spaced apart by 300 μm in a hydrogel sample. Additionally, Whitehill *et al.*¹⁹ showed that low frequency bulk acoustic waves can be used to manipulate particles (40–120 μm) inside a droplet. In all of these cases,^{6–19} ultrasonic bulk waves were used to manipulate the micro-sized features.

Several researchers have used surface acoustic waves (SAWs) (Rayleigh waves) to manipulate microparticles (e.g., Refs. 20–22). SAW devices are typically manufactured by depositing gold plated interdigital transducers on a piezoelectric substrate such as lithium niobate, lithium tantalite, or quartz.²³ These devices can operate in the megahertz or even gigahertz range.²⁴ The SAW devices allow generating standing SAWs on the piezoelectric substrate, and particles can be manipulated into patterns corresponding to the nodes or antinodes formed by these waves (similar to the case of bulk waves). Many publications can be found on acoustic manipulation of cells in microfluidic devices. For instance, Shi *et al.* demonstrated the use of SAW devices to create line and rectangular patterns with cells and microparticles,²¹ and they devised a microfluidic channel for continuous particle separation.²² Very few studies are available in the open literature on manipulating nanosized structures using SAWs. Strobl *et al.*²⁵ showed that SAWs can be used to align multiwalled carbon nanotubes, and Seeman *et al.*²⁶ demonstrated that single walled carbon nanotubes can be manipulated with SAWs to make a connection between gold contacts.

To the best of our knowledge, no published data exist of manipulating suspended nanoparticles in a fluid using bulk acoustic waves, and depositing these patterns on a substrate. This paper attempts to fill this gap and presents a simple “bench top” approach to creating patterns of nanoparticles (diameter of 5 nm) on a substrate using bulk waves instead of SAWs. The patterns are first formed in the bulk of the fluid contained in a reservoir, and then deposited on the substrate due to gravity. This pattern then attaches itself to the substrate as the host fluid evaporates. Additionally, we com-

^{a)}Electronic mail: braeymae@alum.mit.edu.

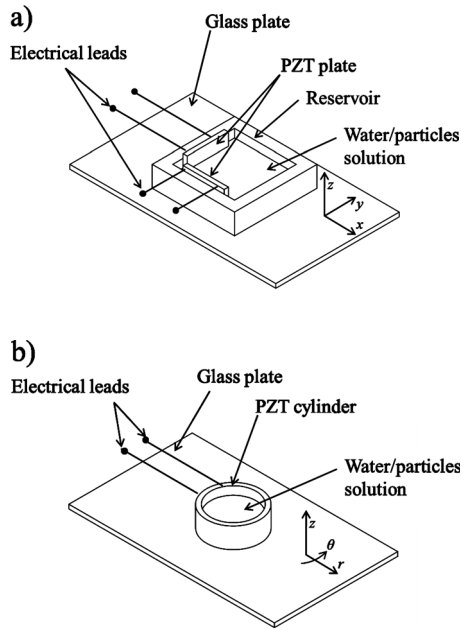


FIG. 1. Experimental apparatus, (a) square reservoir and (b) cylindrical reservoir.

pare existing theoretical models of the acoustic radiation force acting on millimeter-sized and micrometer-sized particles, to our experimental results with nanoparticles. Finally, we discuss the balance between acoustic radiation and drag force acting on a nanoparticle, and determine limits for the particle size that can be manipulated based on particle and fluid properties.

II. EXPERIMENTAL APPARATUS

We have studied manipulating nanoparticles in rectangular as well as in concentric patterns. Figure 1 shows the experimental apparatus we have used for this study. Figure 1(a) shows a square Plexiglas reservoir (length 15 mm, depth 5 mm). Two rectangular plates of lead zirconate titanate (PZT)-5 material (length 10 mm, height 6 mm, 1 mm thick) were mounted on two inner walls of the square reservoir as indicated in Fig. 1(a). Figure 1(b) displays a similar setup consisting of a short length of a piezoelectric (PZT-5) cylinder (inner diameter 10 mm, depth 5 mm, 1 mm thick) glued on a glass plate. The center resonance frequency of both the PZT cylinder and the PZT plates is 2 MHz and was related to the thickness of the PZT material. These resonators were driven using a continuous sine wave by a signal generator (<10 V pk-pk) without any amplifier to create pressure waves inside the respective reservoirs. The reservoirs are filled with a disperse solution of water and nanoparticles. The initial fluid level in the reservoirs was 3 mm. An optical microscope was positioned directly above the reservoirs to image the formation of patterns of nanoparticles.

We have used spherical diamond nanoparticles with a diameter of 5 nm (UltraDiamond96, obtained from Ultradiamond Technologies, Inc.). The diamond nanoparticles contain 96% diamond, the remaining 4% consists of graphite and amorphous carbon. The diamond nanoparticles were not treated with a surfactant to keep them dispersed in the solu-

TABLE I. Maximum acoustic pressure for different frequencies.

| Frequency (MHz) | Pressure (Pa) |
|-----------------|--------------------|
| 1 | 7.65×10^4 |
| 2 | 5.02×10^5 |
| 5 | 1.90×10^5 |
| 10 | 4.08×10^5 |

tion. The nanoparticle concentration in the host fluid (water in our case) was chosen to be sufficiently small to make the effect of multiple scattering negligible.²⁷

The acoustic pressure emitted at the source (a single PZT plate) in the square reservoir was measured by a calibrated needle hydrophone (ONDA Corp. HNR-1000, diameter 1.5 mm) for different frequencies at a fixed excitation voltage of 10 V. The small size of the needle hydrophone ensures that the pressure measurement is minimally corrupted by introducing the hydrophone in the reservoir. The second PZT plate was not energized while performing the measurement. The pressure measurements are presented in Table I. The maximum acoustic pressure was observed at the resonance frequency of the PZT crystal (2 MHz) as expected from the frequency response function of the PZT crystal.

III. EXPERIMENTAL RESULTS

Figure 2 shows the results obtained with the square reservoir and two orthogonally oriented PZT plates tuned to their resonance frequency of 2 MHz. In Fig. 2(a) only one PZT plate in a given orientation was used as a source, resulting in line patterns of the nanoparticles assembling at the nodal locations of the standing acoustic wave. In Fig. 2(b) the two orthogonally oriented PZT plates were simultaneously excited. The wavelength in water at 2 MHz is $750 \mu\text{m}$, as indicated in the figure.

Figure 2(b) shows that the particles do assemble at the nodal points of the interference pattern created by the superposition of two orthogonally oriented standing waves, as expected. The patterns were observed over the entire surface in the respective reservoirs. Since the PZT plates do not cover

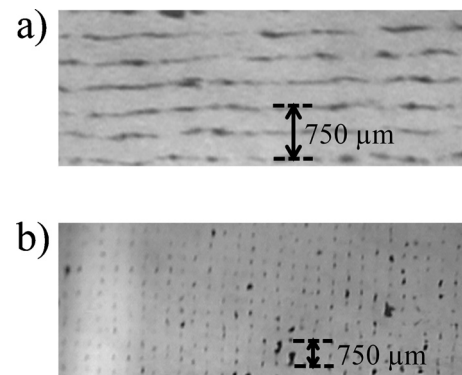


FIG. 2. 5 nm diameter spherical diamond nanoparticles (a) one dimensional acoustic field and (b) two-dimensional acoustic field.

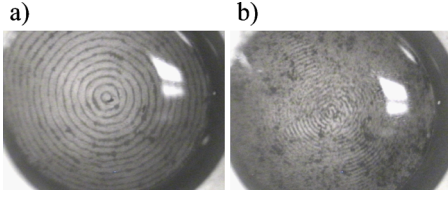


FIG. 3. (Color online) 5 nm diameter spherical diamond nanoparticles in a concentric pattern: (a) 2 MHz and (b) 4 MHz.

the entire wall of the square reservoir [see Fig. 1(a)], minimal boundary effects were observed at the edges of the standing wave interference pattern.

Figure 3 shows the experimental results obtained with the cylindrical PZT reservoir, using a solution of water and 5 nm diamond particles. Standing waves were created in the cylindrical reservoir at frequencies of 2 MHz [Fig. 3(a)], and 4 MHz [Fig. 3(b)], respectively. The pattern formation on the substrate is a two-step process. First the nanoparticles assemble at the nodes of the standing wave pattern in the cylindrical reservoir due to acoustic radiation force (see modeling section of this paper). These patterns then drift downward due to gravity over a small distance (1–3 mm) and settle down on the glass substrate below. As the host fluid evaporates, the pattern becomes attached to the substrate. The spacing of the pattern depends on the frequency used and it becomes more densely spaced with increased frequency.

We observe that the concentric rings and the clusters of nanoparticles in Figs. 2 and 3 are not identical in size, i.e., not all the nodal points in Fig. 2(b) and the nodal concentric circles in Figs. 3(a) and 3(b) collected an equal number of nanoparticles. Therefore, they do not have exactly the same size. This may be the result of a nonuniformly dispersed solution of nanoparticles and water prior to starting the experiment. It is worth pointing out that no acoustic streaming or cavitation was observed during the experiments consistent with the low acoustic pressures used (see Table I).

IV. MODELING

A. Theory

Acoustic radiation force acting on a rigid sphere in a sound field has been studied by many authors^{1–5,28–32} over several decades. Yosioka *et al.*^{28,33} and Gor'kov³⁴ extended these studies by including the compressibility of the sphere. Spherical particles with radius R in a plane, parallel wave sound field [square reservoir Fig. 1(a)] in an inviscid medium will assemble at the minima of the time averaged force potential function \bar{U} , presented by Gor'kov as

$$\bar{U} = \frac{2}{3} \pi R^3 \left[\frac{\bar{p}^2}{\rho_m c_m^2} - \frac{\bar{p}^2}{\rho_p c_p^2} - \frac{3\rho_m(\rho_p - \rho_m)\bar{v}^2}{2\rho_p + \rho_m} \right]. \quad (1)$$

The acoustic radiation force can thus be written as the negative gradient of the force potential $F = -\nabla \bar{U}$, or

TABLE II. Density and compressibility of water and diamond (Refs. 35 and 36).

| | Density (kg/m ³) | Compressibility (Pa ⁻¹) | Sound speed (m/s) |
|---------|---------------------------------|--|----------------------|
| Water | 1000 | 4.44×10^{-10} | 1 500 |
| Diamond | 3515 | 1.98×10^{-12} | 12 000 |

$$F = -\nabla \left(\frac{2}{3} \pi R^3 \left[\frac{\bar{p}^2}{\rho_m c_m^2} - \frac{\bar{p}^2}{\rho_p c_p^2} - \frac{3\rho_m(\rho_p - \rho_m)\bar{v}^2}{2\rho_p + \rho_m} \right] \right), \quad (2)$$

where ρ_m , ρ_p and c_m , c_p are the density and speed of sound of the particle (subscript p) and the medium (subscript m). R is the radius of a particle subject to the acoustic radiation force. Using a rectangular Cartesian coordinate system, $\bar{p}^2 = \bar{p}_x^2 + \bar{p}_y^2$ and $\bar{v}^2 = \bar{v}_x^2 + \bar{v}_y^2$ are the time averaged sound pressure in the medium and the medium displacement velocity, respectively. These terms can also shown to be¹¹

$$\bar{p}^2 = \frac{p_{x0}^2 \cos^2(k_x x)}{2} + \frac{p_{y0}^2 \cos^2(k_y y)}{2} + p_{x0} p_{y0} \cos(k_x x) \cos(k_y y) \cos[(\omega_y - \omega_x)t], \quad (3)$$

$$\bar{v}^2 = \frac{1}{2\rho_m} \left[\frac{k_x^2 p_{x0}^2 \sin^2(k_x x)}{\omega_x^2} + \frac{k_y^2 p_{y0}^2 \sin^2(k_y y)}{\omega_y^2} \right], \quad (4)$$

with p_{x0} and p_{y0} the peak pressure amplitudes, $k_x = 2\pi/\lambda_x$, $k_y = 2\pi/\lambda_y$, ω_x , ω_y , λ_x , λ_y the wave numbers, angular frequencies and wavelengths in the x and y direction, respectively. Equation (2) can be shown to reduce to

$$F_x = \frac{\pi R^3}{3} p_{0x}^2 k_x \beta_m \phi \sin(2k_x x), \quad (5)$$

when only considering acoustic pressure along the x -direction. $\beta_m = 1/\rho_m c_m^2$ is the compressibility of the medium. The sign of the acoustic contrast factor Φ indicates whether particles in a dispersed solution will accumulate at the nodes ($\Phi > 0$) or antinodes ($\Phi < 0$) as a result of the acoustic radiation force associated with the standing ultrasound wave pattern.²⁸

$$\Phi = \frac{5\rho_p - 2\rho_m}{2\rho_p + \rho_m} - \frac{\beta_p}{\beta_m}, \quad (6)$$

where $\beta_p = 1/\rho_p c_p^2$ is the compressibility of the particle.

Table II summarizes the respective values of density, compressibility, and sound speed of diamond and water. Using these values in Eq. (6) we find that $\Phi = 1.94$, indicating that the particles assemble at the nodes of the standing ultrasound wave pattern, and implying that repulsive forces will exist at the pressure antinodes. Since the compressibility of the medium is two orders of magnitude larger than the compressibility of the diamond particle, the second term in Eq. (6) is insignificant.

When using a cylindrical reservoir, Gor'kov's theory for plane waves is no longer valid. When only considering waves propagating in the radial direction the time-averaged force potential function \bar{U} is given in polar coordinates as^{32,37}

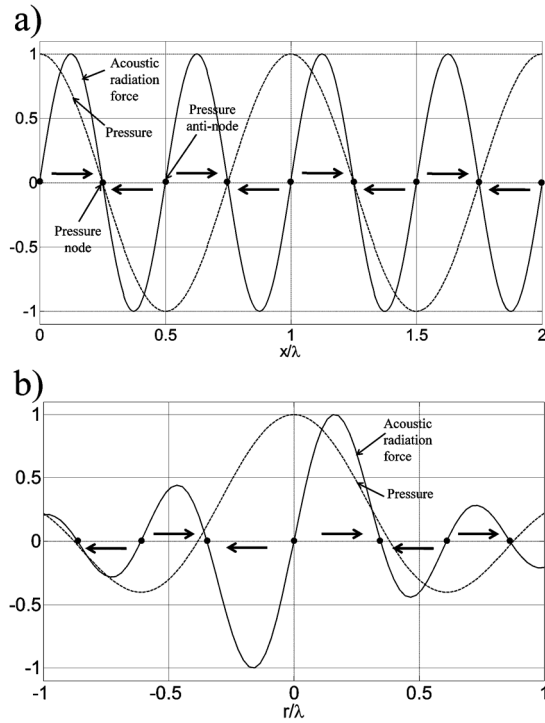


FIG. 4. Variation in the normalized acoustic radiation force and the normalized acoustic pressure for a positive acoustic contrast factor along the axis of the acoustic beam for (a) a square reservoir (with $x/\lambda=0$ at the wall of the reservoir) and (b) a cylindrical reservoir (with $r/\lambda=0$ at the central axis of the reservoir). Arrows indicating the movement of the nanoparticles as a result of the acoustic radiation force.

$$\bar{U} = \frac{\pi R^3 p^2}{3 \rho_m c_m^2} \left[\left(1 - \frac{\rho_m c_m^2}{\rho_p c_p^2} \right) J_0^2(kr) - \frac{3(\rho_p - \rho_m)}{2\rho_p + \rho_m} J_1^2(kr) \right]. \quad (7)$$

The solution is axisymmetric and, thus, independent of θ . J_0 and J_1 are Bessel functions of the first kind and zero and first order, respectively. $k=2\pi/\lambda$ is the wave number and λ the wavelength associated with the pressure wave in the cylindrical reservoir. r is the radial coordinate, as indicated on the coordinate system in Fig. 1(b). The origin is located at the center of the cylindrical reservoir. The acoustic radiation force can thus be written as $F = -\nabla \bar{U}$, which yields^{32,37}

$$F = \frac{\pi R^3 p^2}{3 \rho_m c_m^2} \left\{ \left[2 \left(1 - \frac{\rho_m c_m^2}{\rho_p c_p^2} \right) + \frac{3(\rho_p - \rho_m)}{2\rho_p + \rho_m} \right] J_0(kr) - \frac{3(\rho_p - \rho_m)}{2\rho_p + \rho_m} J_2(kr) \right\} J_1(kr), \quad (8)$$

with J_2 a Bessel function of the first kind and second order. The relationship between the time averaged pressure and radial coordinate r can be expressed as^{32,37}

$$\bar{p}^2 = \frac{p_0^2}{2} J_0^2(kr) \quad (9)$$

Figure 4 presents the variation in the acoustic radiation force (solid line) and the acoustic pressure (dashed line) over two wavelengths. The amplitude of both pressure and acoustic radiation force has been normalized. Figure 4(a) shows the case of a plane wave and a positive acoustic contrast factor using Gor'kov's model (square reservoir with $x/\lambda=0$

at the wall of the reservoir), while Fig. 4(b) depicts the case of a cylindrical reservoir (with $r/\lambda=0$ at the central axis of the reservoir). The horizontal solid arrows indicate the movement of the nanoparticles subject to the acoustic radiation force. Particles are forced along the positive x -axis for a positive acoustic radiation force and vice versa. Thus, particles will collect at locations where the acoustic radiation force is zero. In the case of the rectangular pattern, the locations where the force is zero coincide with pressure nodes.

Note that the acoustic pressure in the case of a radial pressure field achieves a maximum in the center of the circular reservoir, thereby creating a strong focusing effect.

B. Comparing model and experimental results

Figure 5 compares the predictions from Gor'kov's model and the experimental results obtained with 5 nm diamond spheres in water (square reservoir). Figure 5(a) illustrates the force potential \bar{U} [Eq. (1)], resulting from the superposition of two orthogonally oriented cosine functions with identical amplitude, frequency and phase. These results are displayed for four wavelengths in both x and y direction. Figure 5(b) is a magnification of Fig. 5(a) showing only a single wavelength in x and y direction. The force field [Eq. (2)] is indicated by arrows in Fig. 5(b). The length of the arrows is proportional to the magnitude of the acoustic radiation force, while the orientation of the arrow indicates the direction of the force. According to Gor'kov's model, the particles collect at two locations per wavelength, corresponding to the minima of the force potential [Eq. (1)]. The minima are indicated in Fig. 5(b) by solid dots. Figure 5(c) is an expanded view of a small section of Fig. 2(b) (range of four by four wavelengths). The image has been converted to a binary image to accentuate the locations where the 5 nm diamond spheres accumulate. Overlapping Figs. 5(a) and 5(c) in Fig. 5(d) illustrates the good agreement between the experimental results obtained with the nanoparticles and the simulation using Gor'kov's model.

Figure 6 provides a comparison between the model predictions and the experimental results obtained with 5 nm diamond spheres in water for the cylindrical reservoir. Figure 6(a) shows the force potential \bar{U} derived from Eq. (7). The results are shown over a spatial extent of four wavelengths across the diameter of the reservoir. The arrows indicate the concentric circles where the nanoparticles will accumulate. Figure 6(b) is an expanded view of Fig. 6(a), showing a single wavelength centered around the central axis of the cylindrical reservoir. The force field [Eq. (8)] is indicated by arrow vectors in Fig. 6(b). The spacing between the concentric circles where particles collect does not remain constant across the diameter of the reservoir because the spacing between zeros of the Bessel function of the first kind is not constant [see Eq. (7)]. The minima are indicated in Fig. 6(b) as a solid black circle. Figure 6(c) is an extract from Fig. 2(b). As before, the image has been converted to a binary image to accentuate the locations where the 5 nm diamond spheres accumulate. Consistent with the previous case of rectangular geometry, there is very good agreement between the experi-

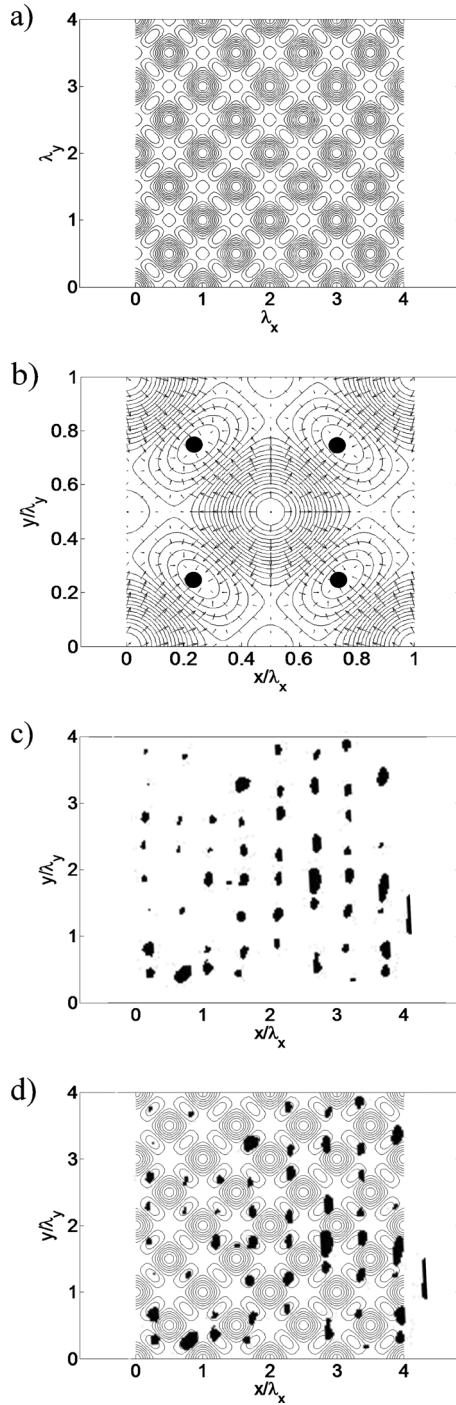


FIG. 5. Force potential for spherical diamond nanoparticles with a diameter of 5 nm in water in a rectangular reservoir (a) four wavelengths and (b) one wavelength. Arrows indicate the negative gradient of the force potential, i.e., the acoustic radiation force, (c) extract of Fig. 2 (four wavelengths), converted into a binary image, (d) overlap of theoretical and experimental results.

mental results obtained with the nanoparticles and the simulation as can be seen from a comparison between Figs. 6(a) and 6(c) in Fig. 6(d).

Note that in Fig. 6(c), the concentric rings of particles are not perfectly separated from each other, and few particles seem to float in between the rings.

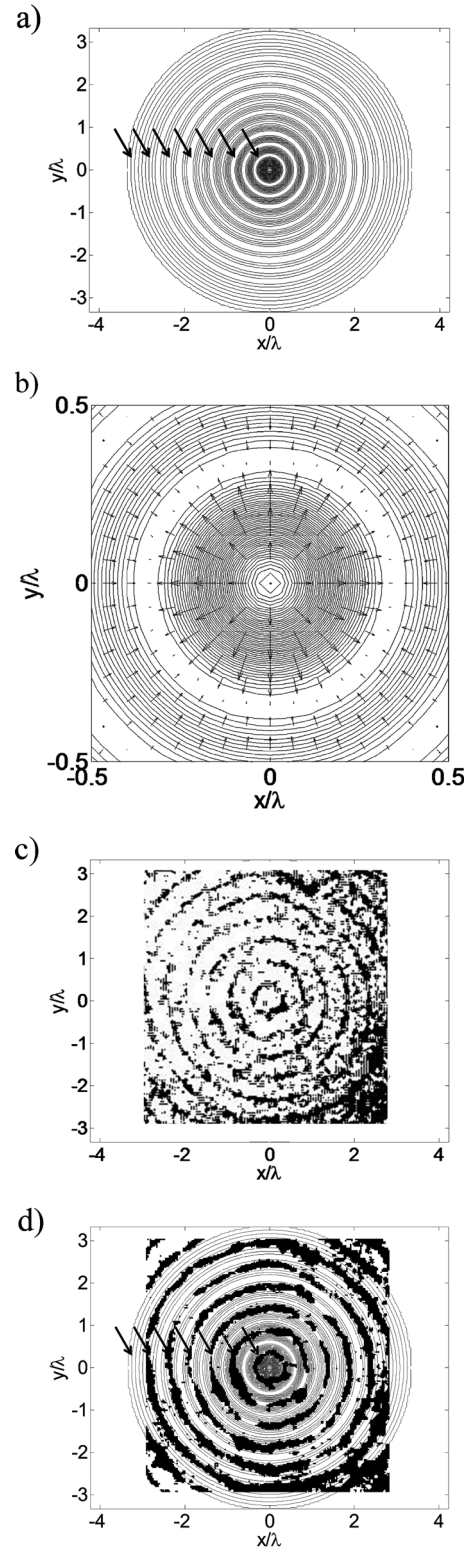


FIG. 6. Force potential for spherical diamond nanoparticles with a diameter of 5 nm in water in a cylindrical reservoir (a) four wavelengths and (b) one wavelength. Arrows indicate the negative gradient of the force potential, i.e., the acoustic radiation force, (c) extract of Fig. 3 (four wavelengths), converted into a binary image, (d) overlap of theoretical and experimental results.

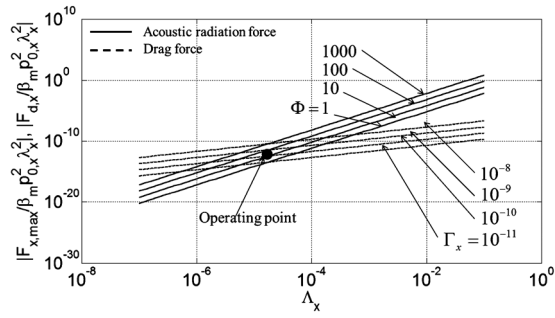


FIG. 7. Nondimensional maximum acoustic radiation force (x -direction) vs nondimensional particle radius for different values of the acoustic contrast factor.

C. Acoustic radiation force versus drag force (in the case of plane waves)

For the rectangular geometry case, using Eq. (5), the maximum force acting on a particle along the x -axis is

$$F_{x,max} = \frac{\pi R^3}{3} p_{0x}^2 k_x \beta_m \phi. \quad (10)$$

By defining a nondimensional particle radius

$$\Lambda_x = R/\lambda_x, \quad (11)$$

Equation (10) can be rewritten in nondimensional form as

$$\frac{F_{x,max}}{\beta_m p_{0x}^2 \lambda_x^2} = \frac{2}{3} \pi^2 \Lambda_x^3 \phi. \quad (12)$$

The acoustic radiation force [Eq. (12)] drives the nanoparticles toward the nodes or antinodes of the standing wave pattern, depending on the sign of the acoustic contrast factor ϕ . While moving, the nanoparticles are subject to a drag force, which can be expressed as^{29,38}

$$F_{d,x} = -6\pi\eta R v_x, \quad (13)$$

with η the viscosity of the medium and v_x the particle velocity in the x -direction. By defining a nondimensional particle velocity

$$\Gamma_x = v_x/c_m, \quad (14)$$

Equation (13) can be re-written in nondimensional form as

$$\frac{F_{d,x}}{\beta_m p_{0x}^2 \lambda_x^2} = -\frac{6\pi\eta c_m \Gamma_x}{\beta_m p_{0x}^2 \lambda_x} \Lambda_x. \quad (15)$$

Figure 7 shows a double logarithmic plot of the nondimensional maximum acoustic radiation force ($F_{x,max}/\beta_m p_{0x}^2 \lambda_x^2$) (x -direction) versus the nondimensional particle radius Λ_x for different values of the acoustic contrast factor ϕ (solid lines). Figure 7 also shows the nondimensional drag force acting on a nanoparticle while it is moving under the influence of the acoustic radiation force, versus the nondimensional particle radius Λ_x , for different values of the nondimensional particle velocity Γ_x (dashed lines). The acoustic pressure used to obtain this graph was chosen equal to the maximum pressure at the resonance frequency of the piezocrystal (500 kPa, see Table I).

From Fig. 7 we observe that the nondimensional maximum acoustic radiation force increases with increasing par-

ticle radius, and with increasing values of the acoustic contrast factor ϕ . We also observe that the nondimensional drag force increases with increasing particle radius and with increasing values of the nondimensional particle velocity Γ_x . The intersections of the respective force and drag curves mark the limits of particle sizes that can be manipulated (for a particular ϕ and Γ_x). The operating point for the rectangular pattern experiment is indicated with a black dot. We observe that in the present situation ($\Phi=1.9$) a particle speed of $\Gamma_x=10^{-10}$ can be obtained.

V. DISCUSSION

A. Gor'kov's model

It is interesting to note that Gor'kov's model is valid for nanoparticles as well as for microparticles. More complex models that account, for e.g., single and multiple scattering, acoustic streaming, Brownian motion, and viscosity exist in the literature. However, Gor'kov's model showed good agreement with the experimental results that were obtained with the 5 nm diamond spheres. Coating the nanoparticles with a surfactant may improve the agreement between Gor'kov's model and the experimental results shown in this paper, because it would allow the experiment to begin from a uniformly dispersed solution of water and nanoparticles.

B. Collecting particles

While in the case of microparticles the separation between host fluid and particles occurs quasi-instantaneously, it takes on the order of seconds or even minutes to separate the nanoparticles from the host fluid at the nodal locations of the standing wave pattern. Figure 7 provides some clarification. The magnitude of the acoustic radiation force must exceed the magnitude of the corresponding drag force for a particle to move. Since the vast majority of the particles are far away ($\gg 2R$) from the substrate when creating the pattern, we have used the Stokes drag force equation [Eq. (13)] rather than accounting for the wall-effect³⁸ that is experienced by only few particles in close proximity ($< 2R$) to the substrate while being driven to the pressure nodes. From Fig. 7 we observe that for small values of $\Lambda_x (< 10^{-5})$, which corresponds to nanoparticles in a 1 to 10 MHz acoustic field, the magnitude of the acoustic radiation force may not be large enough to overcome the drag force. The magnitude of the acoustic radiation force can be increased by choosing a high acoustic contrast factor. This can be obtained by choosing particles with high density and low compressibility compared to the host fluid. Additionally, the magnitude of the acoustic radiation force can be increased by increasing the acoustic pressure at the source. This implies that the solid curves representing the acoustic radiation force in Fig. 7 would shift upwards with increasing source pressure.

The velocity at which the nanoparticles move through the host fluid is slow. For instance, $\Gamma_x=10^{-10}$ corresponds to a speed of 0.15 $\mu\text{m/s}$ in water under atmospheric conditions. This low velocity corresponds to the experimental observations. For a 2 MHz acoustic wave in water, the wavelength corresponds to 750 μm . The maximum travel of the particles is a quarter wavelength or 187.5 μm (see Fig. 4).

At a speed of $0.15 \mu\text{m/s}$ it would thus take 1250 s for the furthest particle to reach the pressure node. This time estimate matches the observation during the experiments well. As a result of the secondary acoustic radiation force (Bjerknes force²⁷) the nanoparticles are attracted to each other when they are forced into close proximity. The acoustic radiation force is no longer acting on a single particle but on a cluster of particles with a larger radius Λ_x than the radius of an individual particle. Hence, the magnitude of the acoustic radiation force increases relative to the drag force (radiation force $\sim R^3$, drag force $\sim R$), thereby increasing the speed of separation. $\Gamma_x = 10^{-11}$ corresponds to a speed of 15 nm/s in water under atmospheric conditions. It is clear that while the particles are still being driven to the pressure nodes of the standing wave pattern, the separation would take too long, unless clustering as a result of the secondary Bjerknes force would increase Λ_x and, thus, accelerate the particle separation from the host fluid. Because the separation of nanoparticles in the host fluid occurs slower than in the case of microparticles, this technique is less suitable to use for a continuous separation process of nanoparticles than a continuous separation of microparticles (e.g., flow cytometry^{39,40}).

From Fig. 3 it is clear that the pattern created at the second harmonic of the source [Fig. 3(b)] is more distorted than the one created at the center frequency of the source [Fig. 3(a)]. According to Eq. (10) the acoustic radiation force is proportional to the source frequency. However, the attenuation of a pressure wave in water is proportional to the square of the frequency. The net result is that it becomes more difficult to create undistorted patterns for increasing frequency, especially further away from the source (effect of increased attenuation dominates).

C. Brownian motion

Brownian motion is an important topic when manipulating nanoparticles. The diffusion coefficient D depends on the particle size R , the temperature T , and the liquid viscosity η . This relationship can be expressed as⁴¹

$$D = \frac{k_B T}{6\pi R \eta} \quad (16)$$

where k_B is the Boltzmann constant. The root mean square (rms) displacement $\langle x \rangle$ of a particle in the x -direction as a result of Brownian motion is given by⁴¹

$$\langle x \rangle = \sqrt{2Dt}, \quad (17)$$

where t is the time. Combining Eqs. (16) and (17) and non-dimensionalizing the result with a quarter wavelength we find,

$$\frac{4}{\lambda_x} \langle x \rangle = \frac{4}{\lambda_x} \sqrt{\frac{k_B T}{3\pi\eta c} \frac{1}{\Lambda_x \lambda_x} ct}, \quad (18)$$

Figure 8 shows the nondimensional rms displacement ($4\sqrt{2Dt}/\lambda_x$) as a function of nondimensional time (ct/λ_x) for different values of the nondimensional particle radius ($\Lambda_x = R/\lambda_x$).

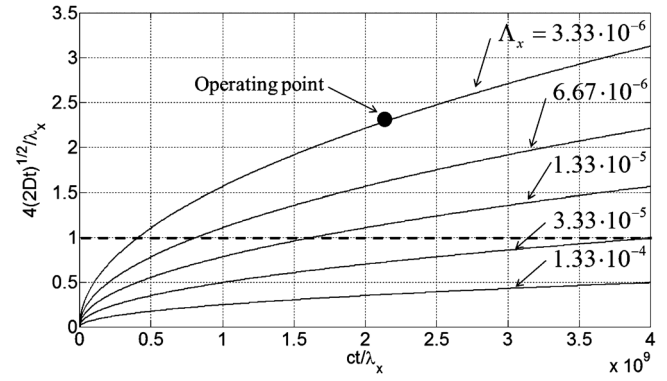


FIG. 8. Nondimensional rms displacement as a result of Brownian motion (x -direction) vs nondimensional time for different values of the nondimensional particle radius.

As expected, the rms displacement due to Brownian motion increases with decreasing particle size and increasing time interval length. The time interval is the travel time needed for a particle to reach a pressure node due to the acoustic radiation force. The dashed line at $4\sqrt{2Dt}/\lambda_x = 1$ indicates the maximum travel distance of a particle toward a pressure node (as discussed in Sec. V B). If the rms displacement $4\sqrt{2Dt}/\lambda_x$ becomes close to 1 for any combination of particle size and time interval, the effect of Brownian motion can become important. The operating point for a 5 nm diamond particle in water in the worst case scenario is indicated in Fig. 8. Here, the distance to a pressure node is a quarter wavelength, i.e., this particle takes the longest to reach the pressure node when exposed to the acoustic radiation force. We note that the rms distance due to Brownian motion is more than twice the travel as a result of the acoustic radiation force. However, starting from a uniform distribution of particles, the initial location of most particles is closer to the pressure node than the worst case (quarter wavelength travel). Thus, these particles take significantly less time to be manipulated toward the node. Additionally, as mentioned earlier, we observed particles forming clusters because of the Bjerknes force acting between particles in close proximity. The “effective” radius of a cluster of particles can be significantly larger than the radius of an individual particle, thereby decreasing the travel time of the particle(cluster) due to the increased acoustic radiation force (proportional to the volume). Simultaneously the effect of Brownian motion (inverse proportional to $\Lambda_x^{1/2}$) is decreased.

D. Pattern deposition

We have deposited the patterns that were formed at the pressure nodes on a glass substrate. The particles are subject to the gravitational force, and will thus be forced toward the glass substrate where they are deposited. Additionally, the fluid in the reservoir evaporates and accelerates the process of depositing the particles on the glass substrate. In our experiments we have used water as a medium with nanoparticles dispersed in it. Other fluids, however, could be used as well, and could be chosen such that the evaporation process is accelerated. When working with small reservoirs one needs to consider the surface tension of the host fluid. If the

contact angle deviates significantly from 90° , the fluid level will not be horizontal. Hence, when the host fluid evaporates the pattern may become distorted. Evidence of this was seen when using acetone as a host fluid rather than water. Patterns can also be formed by capillary flow⁴² (so-called “coffee ring effect”). The results we have obtained by evaporation only (without sound field) indeed evacuated the particles from the center of the cylinder. However, patterns similar to the ones obtained with acoustic standing waves were not observed.

E. Applications

Many applications can be thought of for this technique. It can be used to design two dimensional nanostructured materials, where particles with particular properties can be positioned with prescribed periodicity in a binder matrix. The patterns that are obtained in the host fluid after exposing the mixture to an acoustic field can be deposited on a substrate by allowing the host fluid to evaporate.

VI. CONCLUSION

We have used bulk acoustic waves to manipulate diamond nanospheres in user-defined patterns and we have deposited these patterns on a glass substrate. We have found that

- (1) Using bulk waves allows manipulating nanoparticles into clusters that form a user-defined pattern. We have demonstrated rectangular as well as concentric patterns.
- (2) Gor'kov's model for the acoustic radiation force is still valid for nanoparticles, and the predictions of the model agree well with the obtained experimental results.
- (3) By calculating the drag force acting on a nanoparticle as it is moving through the host fluid, and by calculating the magnitude of the acoustic radiation force, it was shown that nanoparticles can be moved through a host fluid by means of the acoustic radiation force. Limits for the size of the nanoparticles that can be moved were established based on the particle and host fluid properties.
- (4) Using bulk waves instead of SAWs has significant advantages (inexpensive, easy, and flexible). Many applications can be thought of to benefit from this technique.

¹P. J. Westervelt, *J. Acoust. Soc. Am.* **22**, 319 (1950).

²J. Wu and G. Du, *J. Acoust. Soc. Am.* **87**, 997 (1990).

³G. R. Torr, *Am. J. Phys.* **52**, 402 (1984).

⁴M. Gröschl, *Acustica* **84**, 632 (1998).

- ⁵J. Lee, S.-Y. Teh, A. Lee, H. H. Kim, C. Lee, and K. K. Shung, *Appl. Phys. Lett.* **95**, 073701 (2009).
- ⁶S. M. Woodside, B. D. Bowen, and J. M. Piret, *AIChE J.* **43**, 1727 (1997).
- ⁷S. M. Woodside, J. M. Piret, M. Gröschl, E. Benes, and B. D. Bowen, *AIChE J.* **44**, 1976 (1998).
- ⁸H. Andersson and A. van den Berg, *Sens. Actuators B* **92**, 315 (2003).
- ⁹W. T. Coakley, D. W. Bardsley, and M. A. Grundy, *J. Chem. Biotechnol.* **44**, 43 (1989).
- ¹⁰W. T. Coakley, J. J. Hawkes, M. A. Sobanski, C. M. Cousins, and J. Spengler, *Ultrasonics* **38**, 638 (2000).
- ¹¹D. Karpul, J. Tapson, M. Rapson, A. Jongens, and G. Cohen, *J. Acoust. Soc. Am.* **127**, 2153 (2010).
- ¹²T. L. Tolt and D. L. Feke, *Chem. Eng. Sci.* **48**, 527 (1993).
- ¹³Z. Mandralis, W. Bolek, W. Burger, E. Benes, and D. Feke, *Ultrasonics* **32**, 113 (1994).
- ¹⁴S. Gupta, D. L. Feke, and I. Manas-Zloczower, *Chem. Eng. Sci.* **50**, 3275 (1995).
- ¹⁵B. Jung, K. Fisher, K. D. Ness, K. A. Rose, and P. Mariella, Jr., *Anal. Chem.* **80**, 8447 (2008).
- ¹⁶S. Oberti, A. Neild, and J. Dual, *J. Acoust. Soc. Am.* **121**, 778 (2007).
- ¹⁷M. Dorrestijn, A. Bietsch, T. Açikalin, A. Raman, M. Hegner, E. Meyer, and C. Gerber, *Phys. Rev. Lett.* **98**, 026102 (2007).
- ¹⁸J. P. Mazzocchi, D. L. Feke, H. Baskaran, and P. N. Pintauro, *Biotechnol. Prog.* **26**, 600 (2010).
- ¹⁹J. Whitehill, A. Neild, T. W. Ng, and M. Stokes, *Appl. Phys. Lett.* **96**, 053501 (2010).
- ²⁰M. K. Tan, J. R. Friend, and L. Y. Yeo, *Lab Chip* **7**, 618 (2007).
- ²¹J. Shi, D. Ahmed, X. Mao, S. Lin, A. Lawit, and T. J. Huang, *Lab Chip* **9**, 2890 (2009).
- ²²J. Shi, H. Huang, Z. Stratton, Y. Huang, and T. J. Huang, *Lab Chip* **9**, 2254 (2009).
- ²³J. G. Gualtieri, J. A. Kosinski, and A. Ballato, *IEEE Trans. Ultrason. Ferroelectr. Freq. Control* **41**, 53 (1994).
- ²⁴S. Lehtonen, V. P. Plessky, C. S. Hartmann, and M. M. Salomaa, *IEEE Trans. Ultrason. Ferroelectr. Freq. Control* **50**, 1404 (2003).
- ²⁵C. J. Strobl, C. Schäflein, U. Beierlein, J. Ebbecke, and A. Wixforth, *Appl. Phys. Lett.* **85**, 1427 (2004).
- ²⁶K. M. Seemann, J. Ebbecke, and A. Wixforth, *Nanotechnology* **17**, 4529 (2006).
- ²⁷X. Zheng and R. E. Apfel, *J. Acoust. Soc. Am.* **97**, 2218 (1995).
- ²⁸K. Yosioka and Y. Kawasima, *Acustica* **5**, 167 (1955).
- ²⁹L. V. King, *Proc. R. Soc. London, Ser. A* **147**, 212 (1934).
- ³⁰W. L. Nyborg, *J. Acoust. Soc. Am.* **42**, 947 (1967).
- ³¹T. Hasegawa and K. Yosioka, *J. Acoust. Soc. Am.* **46**, 1139 (1969).
- ³²M. Barmatz, *J. Acoust. Soc. Am.* **77**, 928 (1985).
- ³³T. Hasegawa and K. Yosioka, *J. Acoust. Soc. Am.* **58**, 581 (1975).
- ³⁴L. P. Gor'kov, *Sov. Phys. Dokl.* **6**, 773 (1962).
- ³⁵*Properties of Diamond*, edited by J. E. Field (Academic, New York, 1979).
- ³⁶L. E. Kinsler and A. R. Frey, *Fundamentals of Acoustics* (Wiley, New York, 1962).
- ³⁷E. G. Lierke, *Acta Acustica* **206**, 206 (2002).
- ³⁸K. Svoboda and S. M. Block, *Annu. Rev. Biophys. Biomol. Struct.* **23**, 247 (1994).
- ³⁹L. A. Kuznetsova and W. T. Coakley, *J. Acoust. Soc. Am.* **116**, 1956 (2004).
- ⁴⁰G. Goddard and G. Kaduchak, *J. Acoust. Soc. Am.* **117**, 3440 (2005).
- ⁴¹S. Chandrasekhar, *Rev. Mod. Phys.* **15**, 1 (1943).
- ⁴²R. D. Deegan, O. Bakajin, T. F. Dupont, G. Huber, S. R. Nagel, and T. A. Witten, *Nature (London)* **389**, 827 (1997).